ORIGINAL PAPER

Single-crystal X-ray diffraction of grunerite up to 25.6 GPa: a new high-pressure clinoamphibole polymorph

Tommy Yong[1,2] · Przemyslaw Dera[1,2] · Dongzhou Zhang[2]

Abstract

High-pressure single-crystal X-ray diffraction experiments were conducted on natural grunerite crystals with composition $(Fe_{5.237}Mg_{1.646}Ca_{0.061}Mn_{0.051}Na_{0.015}Ti_{0.002}Cr_{0.001}K_{0.001})(Si_{7.932}Al_{0.083})O_{22}(OH)_2$ using a synchrotron X-ray source. Grunerite has $C2/m$ symmetry at ambient conditions. The samples were compressed at 298 K in a diamond-anvil cell to a maximum pressure of 25.6(5) GPa. We observe a previously described phase transition from $C2/m$ (α) to $P2_1/m$ (β) to take place at 7.4(1) GPa, as well as a further transition from $P2_1/m$ (β) to $C2/m$ (γ) at 19.2(3) GPa. The second-order Birch–Murnaghan equation of state fit to our compressional data, yielded the values $V_0 = 914.7(7)$ Å^3 and $K_0 = 78(1)$ GPa for α-grunerite, $V_0 = 926(5)$ Å^3 and $K_0 = 66(4)$ GPa for β-grunerite and $V_0 = 925(27)$ Å^3 and $K_0 = 66(13)$ GPa for γ-grunerite. The β–γ phase transition produces a greater degree of kinking in the double silicate chains of tetrahedra accompanied by a discontinuous change in the a and c unit cell parameters and the monoclinic β angle. At 22.8(4) GPa the O5–O6–O5 kinking angle of the new high-pressure $C2/m$ phase is 137.5(4)°, which is the lowest reported for any monoclinic amphibole. This study is the first structural report to show the existence of three polymorphs within an amphibole group mineral. The high-pressure γ-phase illustrates the parallel structural relations and phase transformation behavior of both monoclinic single and double chain silicates.

Keywords Amphibole · Phase transition · High pressure · Single-crystal X-ray diffraction · Diamond anvil cell · Synchrotron source

Introduction

Amphiboles are one of the most important rock-forming mineral groups found in the Earth's crust and upper mantle. They are widespread in altered oceanic crust and subducting slabs in amphibolite, greenschist, and blueschist facies

✉ Tommy Yong
  tyong@hawaii.edu

1 Department of Geology and Geophysics, School of Ocean and Earth Science and Technology, University of Hawaii at Mānoa, 1680 East West Road, POST Bldg, Honolulu, HI 96822, USA

2 Hawaii Institute of Geophysics and Planetology, School of Ocean and Earth Science and Technology, University of Hawaii at Mānoa, 1680 East West Road, POST Bldg, Honolulu, HI 96822, USA

metamorphic rocks. Amphiboles have such unique chemistry that they are useful tools as petrogenetic indicators (Hirschmann et al. 1994). Structural studies of the amphibole group minerals have been well documented at ambient conditions, however, despite their ubiquity, relatively few structural studies have been conducted under high-pressure conditions. Previous high-pressure structural studies have been limited to pressures below 10 GPa (Comodi et al. 1991, 2010; Zhang et al. 1992; Yang et al. 1998; Welch et al. 2007, 2011; Zanazzi et al. 2010; Nestola et al. 2012), whereas higher pressure studies have only involved spectroscopic observations (Iezzi et al. 2006, 2009, 2011; Thompson et al. 2016).

The cummingtonite-grunerite solid solution is of structural significance and interest as this binary join has three different ambient structural phases, orthorhombic *Pnma* anthophyllite (Mg end-member), monoclinic $P2_1/m$ Mg-rich cummingtonites and monoclinic $C2/m$ grunerites. Earlier experiments on the cummingtonite-grunerite solid solution series have shown that grunerite [Fe-end member,

$Fe_7Si_8O_{22}(OH)_2$] undergoes a phase transition from $C2/m$ (α) to $P2_1/m$ (β) with increasing pressure (Yang et al. 1998; Boffa Ballaran et al. 2000), while $P2_1/m$ Mg-rich cummingtonites transforms to $C2/m$ at high temperature (Prewitt et al. 1970).

The amphibole crystal structure is characterized by double chains of silicate tetrahedra which extend along the [001] crystallographic direction. A band of octahedrally coordinated cations, designated by sites M1, M2, M3 and M4, link adjacent chains of silicate tetrahedra, T1 and T2, along the a axis. The main difference between the $C2/m$ and $P2_1/m$ structure, is that the $C2/m$ phase contains one crystallographically distinct O-rotated silicate chain, while the $P2_1/m$ structure contains two double silicate chains, the S-rotated A chain and O-rotated B chain [see Papike and Ross (1970) for a description of S- and O-rotated chains]. Furthermore, the M4 site cation increases its coordination from 6 to 7 after the $C2/m$–$P2_1/m$ phase transition. The structure and crystal chemical relations of amphibole group minerals have been well documented by Papike and Ross (1970), Papike and Cameron (1976), Law and Whittaker (1980) and Hawthorne and Oberti (2007).

Spectroscopic experiments on a synthetic amphibole with composition, $Na(NaMg)Mg_5Si_8O_{22}(OH)_2$ and $P2_1/m$ ambient symmetry, have indicated a possible existence of a new high-pressure phase characterized by a C-centered lattice, with the phase transition likely to occur between 20 and 22 GPa (Iezzi et al. 2006). This new high-pressure phase change may be analogous to the structural changes seen in clinopyroxenes with increasing pressure, however, the previous study did not include structure determination. To shed new light on the nature of the higher-pressure amphibole phases we reinvestigated the compressional behavior of natural grunerite using synchrotron-based single crystal X-ray diffraction experiments. In this study, we report the results of a previously unknown phase transition in natural grunerite between 16.3(3) and 19.2(3) GPa from $P2_1/m$ (β) to $C2/m$ (γ).

Experimental procedures

Chemical analysis

In this study, we used a natural grunerite sample from Moose Mountain Mine, Ontario, Canada with composition $(Fe_{5.237}Mg_{1.646}Ca_{0.061}Mn_{0.051}Na_{0.015}Ti_{0.002}Cr_{0.001}K_{0.001})$ $(Si_{7.932}Al_{0.083})O_{22}(OH)_2$ determined by wavelength-dispersive spectrometry (WDS) using a JEOL Hyperprobe JXA-8500F at 15 keV. Composition was determined through the average of 16 spot analyses on three different single crystals. The samples were homogenous with no zoning as evidenced from the electron backscattered image. All iron was assigned as Fe^{2+} to maintain charge balance, however, the presence of trace amounts of Fe^{3+} is a possibility. Garnet, chromite, albite, diopside, scapolite, sphene glass and orthoclase standards were used.

The chemical formula was calculated based on 23 O atoms as described by Hawthorne and Oberti (2007). This calculation assumes that (O, OH, F, Cl) = 2 apfu and as no F and Cl were detected from the microprobe analysis, we assumed that there were 2 apfu of OH. The results from the microprobe analysis are shown in Table 1.

Ambient-pressure X-ray diffraction

To characterize the ambient pressure crystal structure of the sample used in the high-pressure experiments, a euhedral, platelet crystal, approximately $0.15 \times 0.09 \times 0.02$ mm in size was selected. The crystal was mounted on a Bruker D8 Venture single crystal diffractometer with a Ag IμS microfocus source (0.56089 Å) and PHOTON-II CPAD detector at the University of Hawaii at Manoa's X-ray Atlas Diffraction Laboratory. The X-ray diffraction data were collected from a θ range of 3.077° to 25.547° with completeness to $\theta = 19.665$. Least-squares structure refinement was done with the program SHELXL (Sheldrick 2008). The initial structure model of grunerite from Finger (1969) was used. All atoms were refined using anisotropic atomic displacement parameters. Full occupancy was assumed for the M1, M2, M3, T1 and T2 sites, based on the calculated chemical formula for our sample. Partial occupancy was refined for the M4 site, which is nominally occupied by Fe^{2+} (Hirschmann et al. 1994). The A site was assumed to be unoccupied as stoichiometric grunerite has a vacant A site, despite our crystal having a small amount of Na and K, which occupies the A site. The small amount of Na and K in our crystal is equivalent to < 0.19 of an electron per unit cell, which is too small of a charge to be detected by the difference-Fourier maps in the structure refinement. The structure was refined using the determined chemical formula from the microprobe analysis as a restraint, however, as diffraction experiments cannot resolve small compositional differences, the small amounts of Ti (0.002 apfu) and Cr (0.001 apfu) were ignored. Fe and Mn have similar X-ray atomic scattering factors, and as such, these atoms were grouped together in the refinement. The M1, M2 and M3 sites were only occupied by Mg^{2+} and Fe^{2+}, the M4 site was occupied by Fe^{2+} and Ca^{2+} and the T1 and T2 sites only contained Si. The refinement assumed no substitutional disorder of Mg^{2+} in the M4 site as there is a strong preference for Fe^{2+} and Ca^{2+} in the M4 site (Hirschmann et al. 1994). The determined site occupancies for the four M sites are: M1: $Fe^{2+} = 0.731(4)$, $Mg^{2+} = 0.269$; M2: $Fe^{2+} = 0.560(4)$, $Mg^{2+} = 0.440$; M3: $Fe^{2+} = 0.749(6)$, $Mg^{2+} = 0.251$; M4: $Fe^{2+} = 0.966(4)$, $Ca^{2+} = 0.022(4)$. Based on these values

Table 1 Results from microprobe analyses

Constituent	Wt.%	Range	Stand. dev.	Probe standard[a]	Crystal	Line	Ions/formula
FeO	39.14	38.06–39.9	0.52	Garnet, Verma (Mn)	LiF	Kα	5.237
MgO	6.9	6.47–7.21	0.28	Chromite USNM 117,075	TAP	Kα	1.646
Na_2O	0.05	0.02–0.1	0.02	Albite, Amelia	TAP	Kα	0.015
Al_2O_3	0.44	0.34–0.6	0.07	Chromite USNM 117,075	TAP	Kα	0.083
SiO_2	49.58	49.15–49.93	0.22	Albite, Amelia	TAP	Kα	7.932
CaO	0.36	0.28–0.47	0.05	Diopside-2 (UCLA)	PETH	Kα	0.061
MnO	0.38	0.31–0.49	0.05	Garnet, Verma (Mn)	LiF	Kα	0.051
Cl	0	0–0.02	0.01	Scapolite	PETH	Kα	0
TiO_2	0.02	0–0.05	0.02	Sphene glass	LiFH	Kα	0.002
K_2O	0.01	0–0.02	0.01	Orthoclase (OR-1)	PETH	Kα	0.001
Cr_2O_3	0.01	0–0.02	0.01	Chromite USNM 117,075	LiFH	Kα	0.001
Total	96.8						

[a]Probe standard compositions (Wt.%)

Garnet, Verma (Mn) = SiO_2: 36.88, Al_2O_3: 20.82, FeO: 18.04, CaO: 0.24, MnO: 24.6

Chromite USNM 117075 = Al_2O_3: 9.92, FeO: 13.04, MgO:15.2, MnO: 0.1, TiO_2: 0.12, Cr_2O_3: 60.5, NiO: 0.16, U_2O_3: 0.09

Albite, Amelia = SiO_2: 68.75, Al_2O_3: 19.43, Fe_2O_3: 0.02, Na_2O: 11.7, K_2O: 0.1

Diopside-2 (UCLA) = SiO_2: 55.27, Al_2O_3: 0.05, FeO: 0.94, MgO: 18.29, CaO: 25.47, MnO: 0.1, Na_2O: 0.05, TiO_2: 0.06

Scapolite = SiO_2: 49.78, Al_2O_3: 25.05, FeO: 0.17, CaO: 13.58, Na_2O: 5.2, K_2O: 0.94, Cl: 1.43, CO_2: 2.5, SO_3: 1.32, H_2O^+: 0.21

Sphene glass: SiO_2: 30.65, CaO: 28.6, TiO_2: 40.75

Orthoclase (OR-1): SiO_2: 64.39, Al_2O_3: 18.58, FeO: 0.03, Na_2O: 1.14, K_2O: 14.92, BaO: 0.82, SrO: 0.035, NiO: 0.03, U_2O_3: 0.08, SO_3: 0.03, H_2O^+: 0.08

our refined chemical formula is $(Fe_{5.26}Mg_{1.669}Ca_{0.044})(Si_8)O_{22}(OH)_2$, which is in good agreement with our calculated chemical formula.

High-pressure X-ray diffraction

High-pressure single-crystal X-ray diffraction experiments were performed at beamlines 13BM-C and 13ID-D (GSE-CARS) of the Advanced Photon Source (APS), Argonne National Laboratory. Three separate experiments were conducted on the natural grunerite sample. Run 1 (13BM-C) consisted of 5 pressure steps ranging from 1.13(2) to 7.4(1) GPa, Run 2 (13ID-D) consisted of 6 pressure steps ranging from 9.0(1) to 25.6(5) GPa and Run 3 (13BM-C) consisted of 3 pressure steps at 10.6(2), 19.2(3) and 22.8(4) GPa. In run 1 we observed the known phase transition from α to β, while in run 2 we observed for the first time the novel phase transition from β to γ. Run 3 was used to solve the new γ-grunerite phase. We utilized data from three different runs as there was not enough coverage of reciprocal space in run 2 to solve the new structure.

Two crystals of grunerite with approximate size of 0.065×0.030×0.005 mm were loaded into a 4-pin diamond-anvil cell (DAC) with 400 μm culet diamonds. Each run utilized a different pair of crystals, however, all crystals used in this study came from the same bulk sample. Conical anvils and backing plates (Boehler and De Hantsetters 2004) were used in runs 1 and 3 to increase coverage of reciprocal space. For run 2, standard brilliant cut diamonds anvils with 0.300 mm culets were used on asymmetric backing plates (cubic boron nitride seat towards the X-ray source and tungsten carbide toward the detector). A hole, 0.210 mm in diameter, was drilled through a 0.250 mm thick rhenium gasket that was preindented to 0.040 mm to act as the sample chamber. Two small ruby spheres were placed in the sample chamber together with the sample crystals as a pressure calibrant. Pressure was calculated from the shift of the R1 ruby fluorescence line (Dewaele et al. 2008). The DAC was gas loaded at the GSECARS-COMPRES facility (Rivers et al. 2008) with neon as the pressure medium to ~ 1.37 GPa. After gas loading the sample chamber had shrunk to ~ 0.115 mm in diameter. Ruby fluorescence spectra were measured at each pressure point both before and after the X-ray data collection. Uncertainties in pressures were taken as 2% of the pressure measurement.

High-pressure diffraction experiments conducted at experimental station 13BM-C were performed using a monochromatic X-ray beam with energy of 28.6 keV (0.434 Å), and 1 eV bandwidth, focused with a Kirkpatrick-Baez mirror system to a spot of 0.015 mm x 0.015 mm, measured as full width at half maximum (FWHM). The MAR165 charge-coupled device (CCD) detector was placed roughly

180 mm away from the sample, and ambient LaB_6 powder was used to calibrate the distance and tilting of the detector. The sample was placed at the rotation center of the diffractometer and aligned using an optical microscope. A total angular range from $\varphi = 56°$ to $125°$ (total angular opening of $\pm 34.5°$) was covered during the scans. A series of step and wide-step φ-exposures were collected. Step scans involved $1°$ angular increments, while wide-step scans had $9.8°$ angular increments. The exposure time was at 3 s/°. After collection of step and wide-step φ-exposures at the zero detector position, more wide-step φ-exposures were recorded with the detector rotated about its horizontal axis (2θ) by $20°$ and then with the detector rotated about the vertical axis (ν) by $10°$ and $-10°$. Exposure time for the non-zero detector position was at 6 s/°.

The monochromatic diffraction experiment at 13ID-D was conducted in a similar manner to those performed at 13-BM-C. X-rays with wavelength of 0.295 Å (42 keV) were used with a focused X-ray beam size of 0.003 mm × 0.003 mm. Diffraction images were collected using a MAR165 charge coupled device (CCD) detector, placed at a sample-to-detector distance of approximately 200 mm. The total rotation range around the vertical axis of the instrument (ω) was $\pm 22°$, with step scans covering $1°$ width and exposure time at 0.5 s/°.

Step φ-exposures (13BM-C) and ω-scans (13ID-D) were used in reconstruction of the crystal's reciprocal lattice to determine the unit cell parameters and to index the diffraction pattern. Wide-step φ-exposures and ω-scans were used to determine d-spacings, azimuthal angles around the beam center and peak intensities of each diffraction peak to solve the crystal structure. Data collection were performed following the procedure described by Dera (2007) and Dera et al. (2013), and data were analyzed using the GSE_ADA/RSV program. Integrated peak intensities were corrected for Lorenz, polarization, DAC absorption and sample displacement effects using the methods implemented in GSE_ADA. Because of the high incident energy, low absorption coefficient and negligible sample thickness the effects of sample absorption were ignored. The structure of the β-phase was refined using an initial cummingtonite model from Yang et al. (1998). The structure of the new high-pressure γ-phase at 22.8(4) GPa was solved using the initial ambient pressure model from Finger (1969). Least-squares structure refinement for selected pressures was done with the program SHELXL (Sheldrick 2008). The procedure for refinement of the high-pressure data was similar to the ambient pressure data, however, all atoms in the high-pressure data were refined with isotropic ADPs due to limited coverage of reciprocal space. The site occupancies of all the high-pressure refinements were constrained to those determined from the ambient structure refinement. In some of the high-pressure data, we were unable to locate hydrogen atoms, to keep the refinements consistent, we have opted to have all hydrogen atoms omitted from the high-pressure structural refinement. Details of the crystal structure refinement, unit cell parameters at each pressure, refined fractional coordinates for all the atoms, bond lengths and atomic displacement parameters for selected pressures are given in Tables 2, 3, 4 and 5. Unfortunately, only one pressure point of the new high-pressure phase produced data allowing to solve and refine the structure, due to limited coverage of reciprocal space.

Table 2 Representative single-crystal structure refinement for grunerite at selected pressures

Run no.	0	1	3	3
Beamline	–	13BM-C	13BM-C	13BM-C
Wavelength (Å)	0.560	0.434	0.434	0.434
Pressure (GPa)	0	1.13(2)	10.6(2)	22.8(4)
Temperature (K)	298	298	298	298
θ range for data collection	3.077–25.547	1.501–19.542	1.401–13.796	1.446–23.182
No. of reflections collected	7782	920	669	2466
No. of independent reflections	1795	258	287	257
Reflections violating $C2/m$ S.G			338	
No. of parameters refined	103	42	84	42
Limiting indices	$-14 \leq h \leq 14$	$-14 \leq h \leq 8$	$-4 \leq h \leq 4$	$-6 \leq h \leq 6$
	$-28 \leq k \leq 28$	$-8 \leq k \leq 7$	$-19 \leq k \leq 18$	$-24 \leq k \leq 24$
	$-8 \leq l \leq 5$	$-6 \leq l \leq 6$	$-5 \leq l \leq 5$	$-7 \leq l \leq 7$
Space group	$C2/m$	$C2/m$	$P2_1/m$	$C2/m$
R_{int}	0.0672	0.0611	0.0682	0.1218
Goodness of fit	1.083	1.109	1.139	1.267
wR_2	0.0928	0.1204	0.1587	0.2406
R_1	0.0382	0.0432	0.0592	0.0998

Table 3 Unit cell parameters of grunerite at various pressures

Run	Pressure (GPa)	a (Å)	b (Å)	c (Å)	β (°)	V (Å^3)	Space group
0	0	9.553(1)	18.327(2)	5.3382(8)	101.854(4)	914.74(8)	$C2/m$
1	1.13(2)	9.504(1)	18.24(1)	5.3224(8)	102.04(1)	902.6(8)	$C2/m$
1	2.22(4)	9.445(1)	18.18(1)	5.3097(7)	102.38(1)	891.0(8)	$C2/m$
1	3.63(7)	9.390(1)	18.11(1)	5.2765(8)	102.63(1)	875.8(9)	$C2/m$
1	5.2(1)	9.338(1)	18.03(1)	5.2510(9)	102.86(1)	862.0(8)	$C2/m$
1	7.4(1)	9.261(1)	17.92(1)	5.2196(8)	103.04(1)	844.2(9)	$P2_1/m$
2	9.0(1)	9.226(4)	17.804(1)	5.1898(3)	103.15(1)	830.1(3)	$P2_1/m$
3	10.6(2)	9.18(1)	17.751(2)	5.1694(7)	103.13(2)	820.8(5)	$P2_1/m$
2	12.0(2)	9.107(6)	17.689(2)	5.1524(4)	103.34(2)	807.7(4)	$P2_1/m$
2	16.3(3)	8.956(8)	17.497(2)	5.1040(5)	103.36(2)	778.2(5)	$P2_1/m$
3	19.2(3)	9.332(1)	17.326(2)	4.9456(8)	107.52(3)	762.5(9)	$C2/m$
2	20.6(4)	9.31(1)	17.298(5)	4.9210(9)	108.03(4)	753(1)	$C2/m$
3	22.8(4)	9.287(6)	17.203(1)	4.8989(4)	107.99(1)	744.3(5)	$C2/m$
2	23.0(4)	9.277(9)	17.1759(3)	4.8934(6)	108.25(3)	740.5(8)	$C2/m$
2	25.6(5)	9.243(9)	17.127(4)	4.8706(6)	108.63(3)	730.7(8)	$C2/m$

Results and discussion

Phase transition in grunerite

Three different phases were observed in grunerite on compression to 25.6(5) GPa. A comparison of all three structures is shown in Fig. 1. The previously reported $C2/m$ (α)–$P2_1/m$ (β) transition was observed between 5.2(1) and 7.4(1) GPa and another transformation was detected between 16.3(3) and 19.2(3) GPa. Unit cell parameters of grunerite up to 25.6(5) GPa are listed in Table 3. The new phase transition transformed the symmetry from $P2_1/m$ (β) to a previously unreported structure. This new structure has monoclinic space group $C2/m$ (γ), determined through analysis of systematic absences in the diffraction pattern and, as evidenced through structure solution and refinement. The structure of all three phases have been solved and refined (Table 2).

At 7.4(1) GPa, the observed structure adopts a primitive lattice based on reflections violating the $C2/m$ space group. The α–β phase transition is thus expected to occur between 5.2(1) and 7.4(1) GPa for the studied sample. The examined crystal transformed to the $P2_1/m$ β-phase by 7.4(1) GPa. There is a small slope change in a, b, c and β at the $C2/m$–$P2_1/m$ transition (Fig. 2). In all four unit cell parameters the slope has decreased suggesting a change in the compression mechanism. Yang et al. (1998) estimated that the $C2/m$–$P2_1/m$ transition pressure has a linear dependence on X_{Fe} with the relationship $P_{tr} = -1.23 + 4.52\ X_{Fe}$. Based on this linear dependence, our sample would be expected to transform to β-grunerite at ~2.21 GPa, which is much lower than our reported value. This suggests that the α–β phase transition pressure is affected by other factors in addition to X_{Fe}.

At 19.2(3) GPa, the structure adopts a C-centered lattice again, as determined through the analysis of systematic absences in the diffraction pattern. A similar high-pressure phase was previously indicated in a synthetic amphibole with composition, $Na(NaMg)Mg_5Si_8O_{22}(OH)_2$, by infrared spectroscopy experiments (Iezzi et al. 2006), based on the presence of a single OH-stretching band, however, until now there have been no previous diffraction experiments reported to confirm this and constrain the crystal structure. This new phase adopts a monoclinic structure with space group $C2/m$, with unit cell parameters at 22.8(4) GPa, $a = 9.287(6)$ Å, $b = 17.203(1)$ Å, $c = 4.89(1)$ Å, $\beta = 107.99(1)°$ and V = 744.4(5) Å^3. The β–γ phase transition in grunerite is accompanied by a discontinuous increase in the a unit cell parameter and β angle (Fig. 2). The a unit cell parameter of β-grunerite at 16.3(3) GPa is 8.956(8) Å and in γ-grunerite at 19.2(3) GPa it increases to 9.34(1) Å. Furthermore, β increases from 103.36(2)° to 107.52(1)° across the transition. Sueno et al. (1973) defined the tetrahedral displacement parameter 'd', as the distance between the centers of two opposing six-membered tetrahedral rings, and found a negative linear correlation between d and β. Figure 3 shows a plot of calculated d values against β, and confirms this negative linear relationship. Whittaker (1960) has associated the degree of the closest packing of the tetrahedral chains with an increase in β, which follows directly from Prewitt and Down's 8th rule of thumb on high pressure effects on bonding and coordination number (Prewitt and Downs 1998), that high-pressure structures tend to be composed of closest-packed arrays of atoms.

Table 4 Atomic positional coordinates and atomic isotropic displacement parameters

Pressure (GPa)	Atom	X	y	z	U_{eq}
1.13(2)	M1	0	0.0876(3)	0.5	0.010(1)
	M2	0	0.1778(4)	0	0.010(1)
	M3	0	0	0	0.009(1)
	M4	0	0.2578(3)	0.5	0.010(1)
	Si1	0.2887(2)	0.0836(4)	0.2736(5)	0.006(1)
	Si2	0.2993(2)	0.1680(4)	0.7783(5)	0.006(1)
	O1	0.1151(5)	0.0882(8)	0.208(1)	0.008(1)
	O2	0.1250(5)	0.1718(8)	0.715(1)	0.007(1)
	O3	0.1157(8)	0	0.705(1)	0.009(2)
	O4	0.3824(6)	0.243(1)	0.767(1)	0.013(1)
	O5	0.3512(5)	0.130(1)	0.064(1)	0.011(1)
	O6	0.3513(5)	0.1174(8)	0.558(1)	0.010(1)
	O7	0.3418(9)	0	0.268(1)	0.013(2)
10.6(2)	M1	−0.2535(1)	0.3355(1)	0.4687(7)	0.009(1)
	M2	−0.252(1)	0.4257(2)	0.9697(7)	0.011(1)
	M3	−0.251(1)	0.25	0.9702(9)	0.010(1)
	M4	−0.2604(8)	0.5101(2)	0.4605(6)	0.012(1)
	Si1A	0.044(3)	0.3341(3)	0.248(1)	0.007(2)
	Si1B	0.547(2)	0.8318(3)	0.314(1)	0.009(2)
	Si2A	0.040(3)	0.4207(3)	0.750(1)	0.011(2)
	Si2B	0.558(2)	0.9152(3)	0.819(1)	0.009(2)
	O1A	−0.136(6)	0.3357(6)	0.178(3)	0.013(5)
	O1B	0.362(5)	0.8355(6)	0.234(3)	0.016(4)
	O2A	−0.131(6)	0.4211(7)	0.685(3)	0.018(5)
	O2B	0.370(5)	0.9201(6)	0.745(3)	0.013(4)
	O3A	−0.115(6)	0.25	0.691(4)	0.014(5)
	O3B	0.373(5)	0.75	0.735(3)	0.004(4)
	O4A	0.122(3)	0.5015(6)	0.789(2)	0.005(3)
	O4B	0.631(4)	0.9907(6)	0.750(2)	0.011(3)
	O5A	0.117(4)	0.3662(6)	0.010(3)	0.015(4)
	O5B	0.616(4)	0.8948(6)	0.139(2)	0.009(3)
	O6A	0.117(4)	0.3855(6)	0.512(2)	0.014(3)
	O6B	0.608(5)	0.8513(6)	0.630(3)	0.013(3)
	O7A	0.104(6)	0.25	0.305(3)	0.013(5)
	O7B	0.611(6)	0.75	0.260(3)	0.009(5)
22.8(4)	M1	0	0.0857(2)	0.5	0.005(1)
	M2	0	0.1747(2)	0	0.004(1)
	M3	0	0	0	0.006(1)
	M4	0	0.2638(2)	0.5	0.007(1)
	Si1	0.307(1)	0.0822(2)	0.340(1)	0.006(1)
	Si2	0.301(1)	0.1681(2)	0.833(1)	0.004(1)
	O1	0.135(4)	0.0861(5)	0.236(3)	0.004(3)
	O2	0.121(4)	0.1724(5)	0.735(3)	0.008(3)
	O3	0.139(5)	0	0.738(4)	0.002(3)
	O4	0.380(4)	0.2439(5)	0.759(3)	0.010(2)
	O5	0.363(3)	0.1499(4)	0.184(3)	0.006(2)
	O6	0.368(3)	0.0946(5)	0.690(3)	0.009(3)
	O7	0.363(5)	0	0.267(4)	0.009(3)

Table 5 Bond lengths (Å) for grunerite at selected pressures

Pressure (GPa)	1.13(2)	10.6(2)		22.8(4)
		Set A	Set B	
M1-O1	2.075(6)	2.04(3)	2.01(3)	2.06(3)
M1-O2	2.12(1)	2.06(3)	2.02(2)	2.00(2)
M1-O3	2.112(7)	2.14(3)	2.02(2)	2.07(3)
Average	2.10233	2.04833		2.04333
M2-O1	2.14(1)	2.08(3)	2.05(2)	2.08(2)
M2-O2	2.111(5)	2.04(3)	2.03(3)	1.96(2)
M2-O4	2.06(1)	1.99(2)	2.03(2)	1.94(1)
Average	2.10367	2.03667		1.99333
M3-O1	2.12(1)	2.02(3)	1.99(2)	2.05(2)
M3-O3	2.093(8)	2.12(4)	2.08(3)	2.08(3)
Average	2.1065	2.0525		2.065
M4-O2	2.15(1)	2.15(3)	2.05(3)	2.06(2)
M4-O4	1.985(5)	2.02(2)	1.98(2)	1.94(2)
M4-O5			2.45(1)	2.23(1)
M4-O6	2.73(1)	2.26(2)	2.96(2)	
Average	2.28833	2.26714		2.07667
T1-O1	1.616(6)	1.61(4)	1.66(4)	1.53(4)
T1-O5	1.61(1)	1.63(2)	1.65(2)	1.56(1)
T1-O6	1.631(9)	1.64(1)	1.63(1)	1.64(1)
T1-O7	1.608(7)	1.59(1)	1.61(2)	1.58(1)
Average	1.61625	1.6175	1.6375	1.5775
T2-O2	1.622(6)	1.53(4)	1.68(4)	1.60(4)
T2-O4	1.59(1)	1.61(2)	1.58(2)	1.58(1)
T2-O5	1.64(1)	1.67(2)	1.66(1)	1.66(1)
T2-O6	1.64(1)	1.68(2)	1.63(2)	1.65(1)
Average	1.623	1.6225	1.6375	1.6225

Equation of state, bulk moduli and linear compressibilities

Weighted volume and pressure data from all three phases were used to fit the second-order Birch–Murnaghan (BM) equation of state (EOS) using the program EOS-FIT V7 program (Gonzalez-Platas et al. 2016). The results of the EOS are plotted in Fig. 4 and shown in Table 6. The bulk moduli determined from this study is in good agreement with Yang et al. (1998), the larger V_0 in our study is likely due to greater Fe content in our sample [ionic radius of $^{VI}Mg^{2+} = 0.72$ Å and high spin $^{VI}Fe^{2+} = 0.78$ Å (Shannon 1976)].

Linear compressibilities, defined as $\beta_{l0} = 1/3K_{l0}$ (Angel 2000), were determined by weighted least-squares fit of the linearized second-order BM equation of state (Fig. 2; Table 6). Linear compressibilities for α-grunerite are 0.0052(1), 0.0035(1) and 0.0038(1) GPa^{-1} for β_a, β_b and β_c, respectively, with a ratio of 1.49:1.00:1.10. For the $P2_1/m$ polymorph the axial compressibilities were 0.007(1), 0.0038(3) and 0.00381(2) GPa^{-1} for β_a, β_b and β_c, respectively, with a ratio of 1.86:1.00:0.99. Zhang et al. (1992)

α-grunerite
O-rotated

γ-grunerite
O-rotated
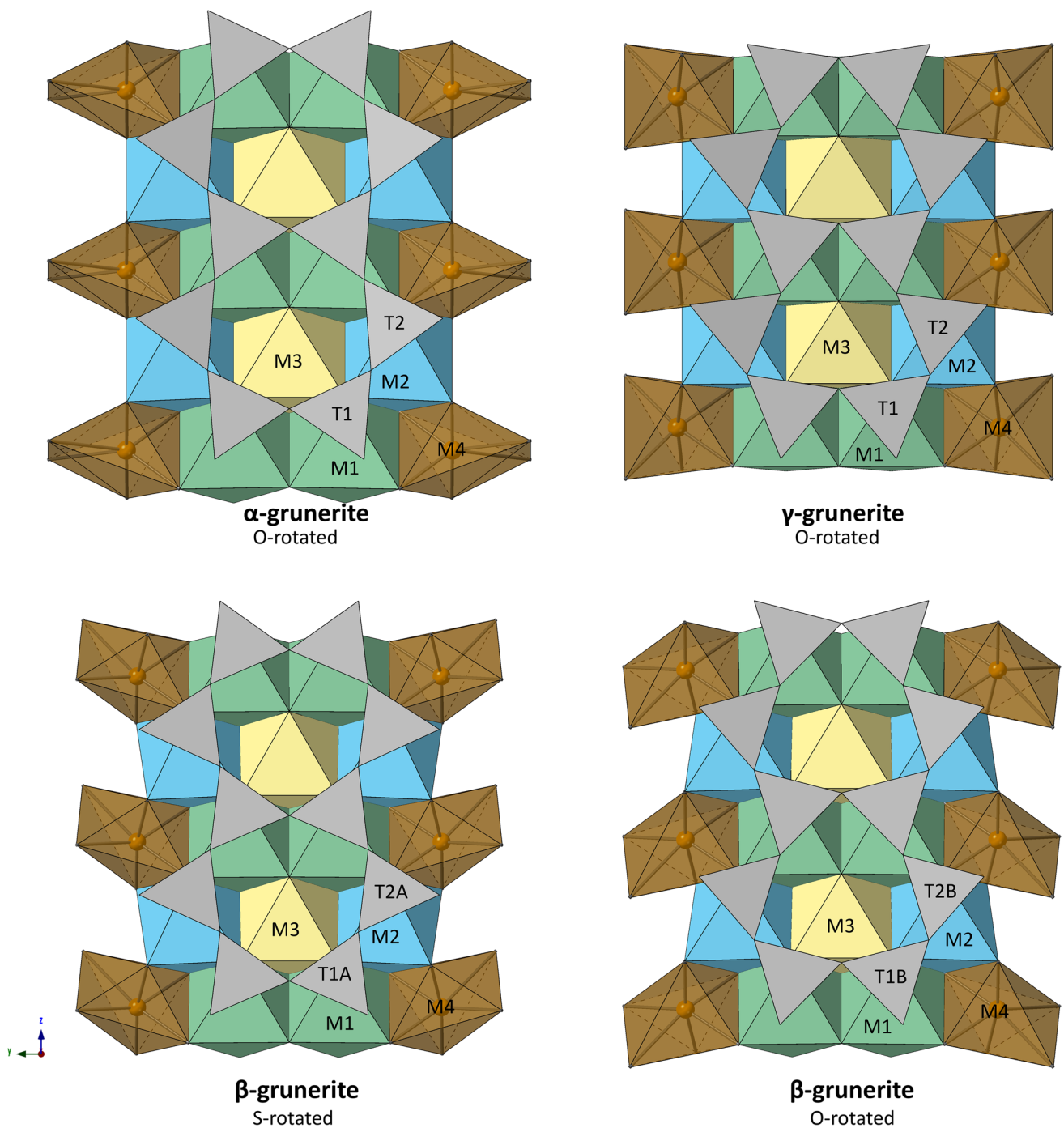
β-grunerite
S-rotated

β-grunerite
O-rotated

Fig. 1 (100) projection of the partial structure of grunerite showing the structural changes across the α–β–γ phase transition. In the α and γ phase the double-chain of tetrahedra are O-rotated. In the β-grunerite phase, the reduction in symmetry causes the double-chains to split into two crystallographically distinct chains, the A-chain (S-rotated) and the B-chain (O-rotated)

reported $\beta_a:\beta_b:\beta_c$ of 1.42:1.00:1.03 for a single-crystal X-ray study on natural grunerite up to 5.1 GPa, which is in good agreement with our reported values for the ambient phase. For the new high-pressure γ-phase the linear compressibilities were 0.0023(4), 0.0040(8) and 0.005(1) GPa^{-1} for β_a, β_b and β_c, respectively, with a ratio of 0.56:1.00:1.41.

All three phases display strong compressional anisotropy. In the ambient pressure and $P2_1/m$ phase the a axis is the most compressible while the b and c axis display similar compressibilities. In the new high-pressure γ-phase the a axis is the least compressible while the most compressible direction is along the crystallographic c axis indicating a
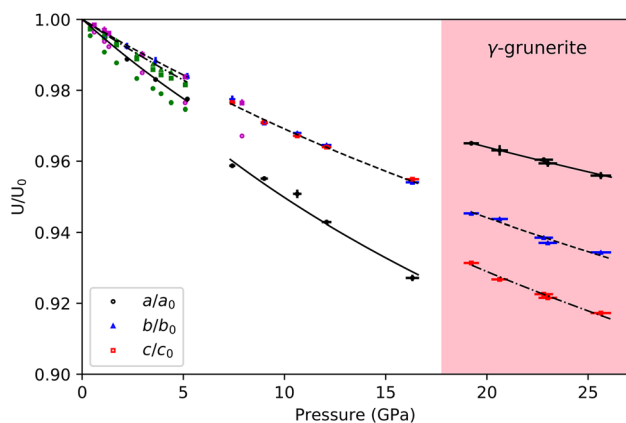
Fig. 2 Normalized unit cell parameters of grunerite from this study (black, blue and red) plotted against pressure. Results from previous experiments are shown in green (Zhang et al. 1992) and magenta (Yang et al. 1998). Results of linearized second order BM EOS fit for each axis are shown with solid, dash-dot and dashed lines for a/a_0 (in black), b/b_0 (in blue), c/c_0 (in red), respectively
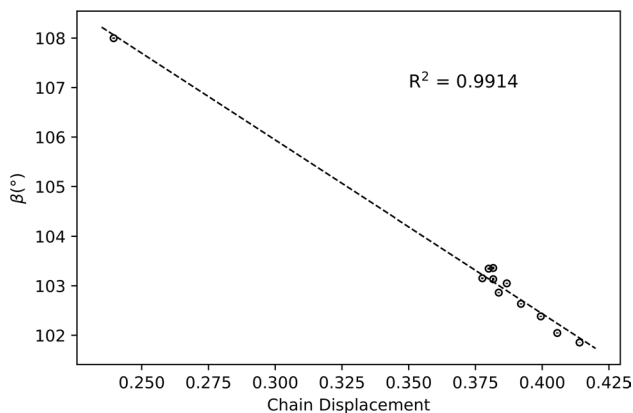

Fig. 4 Unit cell volume of grunerite from this study (black, blue and red), with a second-order BM EOS, compared to previous experiments [green and magenta, Zhang et al. (1992) and Yang et al. (1998), respectively]. Circles, squares and triangles are the ambient pressure α-phase, β-phase and high-pressure γ-phase, respectively

Fig. 3 Relationship between β and the chain displacement factor in grunerite

change in the compression mechanism. It should be noted that the degree of compressional anisotropy increases with each phase transition.

Structural changes with pressure

The kinking angle of the silicate chains are characterized by the O5–O6–O5 angle. With increasing pressure, the kinking angle in α-grunerite decreases from 171.3(1)° at ambient pressure to 168(3)° at 5.2(1) GPa (Fig. 5). During the α–β phase transition, the silicate chain becomes two crystallographically unique chains, the A and B chain. Upon further compression, the A and B chain kinking angle decreases. The A chain kinking angle decreases from 166(4)° at 7.4(1) GPa to 157(1)° at 16.3(3) GPa, while in the B chain it decreases from 146(4)° to 141(1)° at the same respective

pressures. The difference between the kinking angle of the two chains ($\Delta\theta$) decreases from 19.8(5)° to 16.0(5)° from 7.4(1) to 16.3(3) GPa. During compression the sense of rotation of both A and B chains remain the same, the A chain being S-rotated and the B chain O-rotated. The change in rotation type in the A chain to S-type parallels the clinopyroxene $C2/c$ to $P2_1/c$ transition where the A chain is also S-rotated and more extended than the B chain, which is O-rotated and significantly more kinked (Hugh-Jones et al. 1994). Yang et al. (1998) observed a change in the sense of rotation in the A chain from O to S-rotated with increasing pressure, however, our results show that the A-chain remains S-rotated throughout. In the new γ-phase of grunerite, the A and B chain consequently become one distinct chain because of the change in symmetry, geometrically they are both equal to the B chain in the β-phase. Similarly, to the α-phase, the silicate chains in the high-pressure γ-phase are also O-rotated. Of more importance, however, is the change in the kinking angle, which at 22.8(4) GPa is 137.5(4)°.

In clinopyroxenes the HT $C2/c$ structure is characterized by chains that are nearly fully extended, whereas the HP $C2/c$ phase displays tetrahedral chains that are more kinked (Arlt et al. 2000; Yang and Prewitt 2000; Tribaudino et al. 2001, 2003). Correspondingly to the structural changes observed in pyroxenes, the low-pressure $C2/m$ α-grunerite is characterized by silicate chains which are slightly bent from being fully extended [171.3(1)° at ambient pressure], while the high-pressure $C2/m$ γ-grunerite has silicate chains that display more kinking [137.5(4)° at 22.8(4) GPa]. The primitive lattice, β-grunerite phase, is an intermediate structure having two silicate chains displaying different behavior from both the low and high-pressure C-centered polymorphs. The structural evolution of the double silicate chains is shown in

Table 6 Equation of state data for grunerite

References	Phase	Pressure medium	P_{max}(GPa)	K_{0T} (GPa)	K'_{0T}	β_a	β_b	β_c	β_a: β_b: β_c
Zhang et al. (1992)	$C2/m$	4:1 meth-eth	5.1	50(1)	13(1)	0.00497(6)	0.00350(4)	0.0062(5)	1.41:1.00:1.03
Yang et al. (1998)	$C2/m$	4:1 meth-eth	7.9	78(3)	4	0.0068(2)	0.0024(3)	0.0028(1)	2.83:1.00:1.17
Yang et al. (1998)	$P2_1/m$	4:1 meth-eth	7.9	71(1)	6.1(5)	0.0043(3)	0.0029(1)	0.0030(1)	1.48:1.00:1.03
This study	$C2/m$	Ne	25.6(5)	78(1)	4	0.0052(1)	0.0035(1)	0.0038(1)	1.49:1.00:1.10
This study	$P2_1/m$	Ne	25.6(5)	66(4)	4	0.007(1)	0.0038(3)	0.00381(2)	1.86:1.00:0.99
This study	$C2/m$	Ne	25.6(5)	66(13)	4	0.0023(4)	0.0040(8)	0.005(1)	0.56:1.00:1.41

Composition:

Zhang et al. (1992)—$(Fe^{2+}_{5.33}Mg_{1.46}Fe^{3+}_{0.14}Na_{0.05}K_{0.01}Al_{0.01})(Si_{7.92}Al_{0.08})O_{22}(OH_{1.92}F_{0.05}Cl_{0.01})$

Yang et al. (1998)—$(Fe_{3.272}Mg_{3.445}Ca_{0.076}Mn_{0.199}Al_{0.008})(Si_{7.983}Al_{0.017})O_{22}(OH)_2$

This study—$(Fe_{5.237}Mg_{1.646}Ca_{0.061}Mn_{0.051}Na_{0.015}Ti_{0.002}Cr_{0.001}K_{0.001})(Si_{7.932}Al_{0.083})O_{22}(OH)_2$
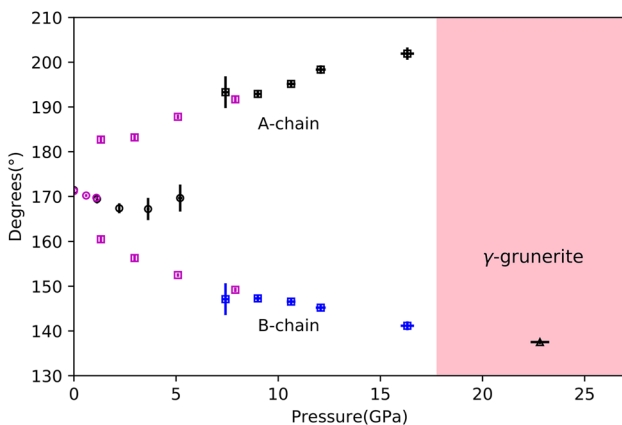
Fig. 5 O5–O6–O5 kinking angle in grunerite as a function of pressure. The kinking angle of the A chain (black squares) are plotted as 360° minus the O5A–O6A–O5A angle to maintain the same analogy with clinopyroxenes. Circles, squares and triangles are the ambient pressure α-phase, β-phase and high-pressure γ-phase, respectively. Blue squares are the B-chain in the $P2_1/m$ phase. Results from Yang et al. (1998) are shown as magenta markers

Fig. 6 Variation of M4–O5 distances in grunerite with pressure. Black squares are M4–O5A distances and blue squares are M4–O5B distances in the β-phase. Results from Yang et al. (1998) are shown as magenta markers

Fig. 1. It is interesting to note, as discussed by Papike and Ross (1970), that with further kinking towards the maximum angle of 120° the hexads of SiO_4 tetrahedra will possess threefold rotation symmetry. Complete O-rotation of the double chains will result in a cubic close packing of oxygen atoms. In the HP $C2/c$ clinopyroxene structure, oxygen atoms also display behavior near that of cubic closest-packing due to the extreme kinking of the silicate chains. While the degree of closest packing in amphiboles can be characterized by an increase in the monoclinic β angle this is not the case for clinopyroxenes. In previous high-pressure experiments on clinopyroxenes, the monoclinic β angle decreases with pressure and has a discontinuous decrease across the $P2_1/c$ to HP $C2/c$ phase transition (Hugh-Jones et al. 1994; Arlt et al. 1998; Tribaudino et al. 2001; Alvaro et al. 2010), this is in contrast with our study where the β angle increases with pressure.
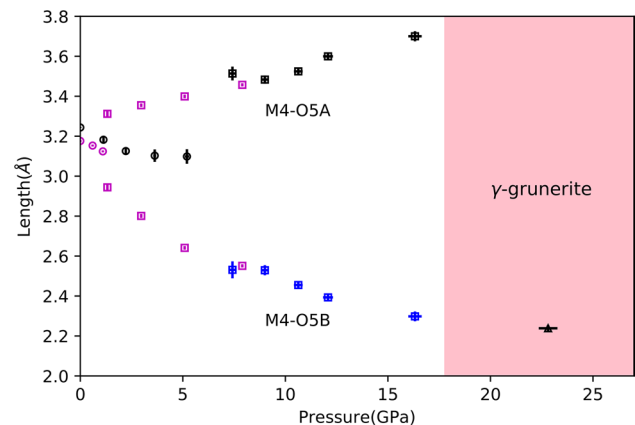
Yang et al. (1998) discussed the correlation between the variation of O5–O6–O5 angle and changes in M4–O5 and M4–O6 distances due to the $C2/m$-$P2_1/m$ phase transition in cummingtonite. The values for M4–O5 and M4–O6 distances are shown in Figs. 6 and 7. Our study is in good agreement with these observations. In the $P2_1/m$ β-phase, the M4–O5A distance increases with pressure from 3.50(4) Å at 7.4(1) GPa to 3.70(2) Å at 16.3(3) GPa, while the M4–O5B distance decreases across the same pressure range from 2.54(5) Å to 2.31(2) Å. This is due to the increase in coordination from six to seven in the M4 site as the structure transitions from the α-phase to the β-phase. The kinking of the silicate chain pushes the O5B atom to coordinate with M4 while O5A moves further away. With increasing pressure as the structure changes from $P2_1/m$ to the high-pressure $C2/m$ γ-phase the M4–O6 distance is significantly increased to 3.00(1) Å due to further kinking of the tetrahedral chains. The coordination number in M4 decreases to six across the phase transition, as the O6 atom moves
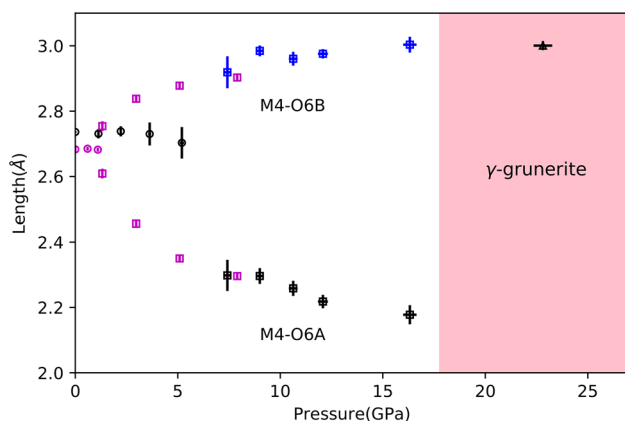
Fig. 7 Variation of M4–O6 distances in grunerite with pressure. Black squares are M4–O6A distances and blue squares are M4–O6B distances in the β-phase. Results from Yang et al. (1998) are shown as magenta markers

to the M2 polyhedron in pyroxenes, which also displays similar properties. In the HP $C2/c$ clinopyroxene phase, the extreme kinking of the silicate-chain involves breaking of bonds between O3 and M2 atoms, as a consequence, the M2 site no longer shares any edges with the silicate chain (Hugh-Jones et al. 1994; Downs 2003). In a similar manner, in γ-grunerite the extreme kinking of the double silicate chains leads to no sharing of edges between the SiO_4 tetrahedra and the M4 polyhedron.

Implications

The close similarities of the physical, chemical and crystallographic properties between amphiboles and pyroxenes have been known for quite some time (Warren 1930; Warren and Modell 1930). Carpenter (1982) determined that the high-temperature to low-temperature displacive transformations in amphiboles and pyroxenes to be exactly analogous, even in the resulting microstructures. The non-ambient behavior of clinopyroxenes have been well studied across a wide variety of compositions (Brown et al. 1972; Smyth 1974; Hugh-Jones et al. 1994; Arlt and Armbruster 1997; Arlt et al. 1998, 2000; Yang and Prewitt 2000; Tribaudino et al. 2001, 2003; Nestola et al. 2008; Alvaro et al. 2010). These studies have shown that clinopyroxenes undergo a series of phase transformations from the high-temperature-$C2/c$ to $P2_1/c$ to high-pressure-$C2/c$ phase. Based on their comparable behavior, a similar series of phase transitions is expected in clinoamphiboles. Our single-crystal experimental data have shown the existence of a new phase of grunerite above 19.2(3) GPa. This study is the first structural report to show the existence of three polymorphs within an amphibole group mineral, which closely mirrors the phase transition sequence in clinopyroxenes as mentioned above. The existence of the γ-phase of grunerite illustrates the corresponding
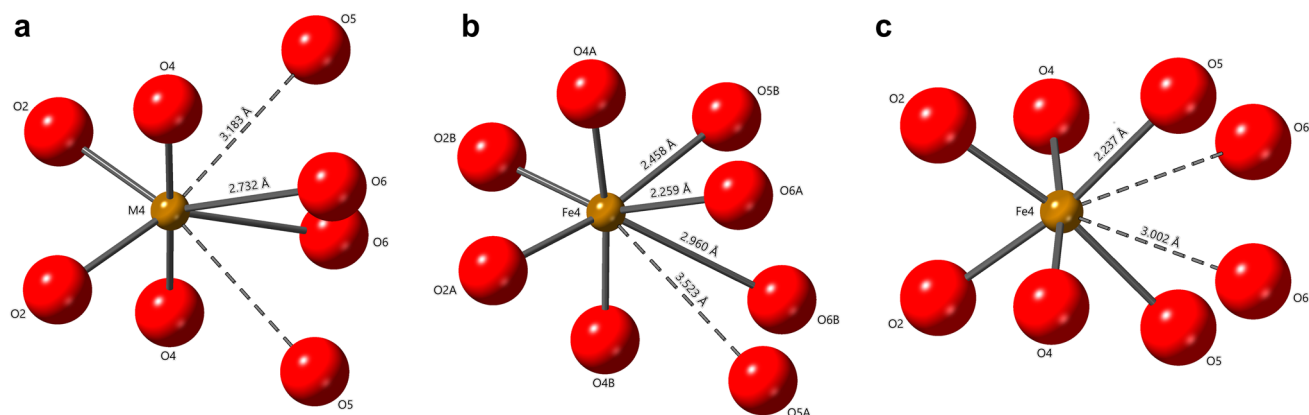
further away from the coordination sphere, whereas the O5 atom moves closer in Fig. 8. In the α-phase the M4 shares five edges with surrounding polyhedra (Fig. 9). Two edges are shared with the M2 polyhedra, one edge with the M1 polyhedron and two edges with T2 polyhedra. In the β-phase the M4 shares an additional edge with the T2A tetrahedron, decreasing the stability of the ionic structure due to the increase in cation–cation repulsion as per Pauling's third rule. During the β–γ phase transition, as the M4 coordination number decreases back to six, the stability of the polyhedral configuration increases, as the number of shared edges decreases from six in β-grunerite, to three in γ-grunerite. In the γ-phase, the M4 polyhedron shares two edges with the M2 polyhedra and one edge with the M1 polyhedron. As the M4 site in amphiboles are considerably more distorted than the M1, M2 and M3 sites and are generally filled with relatively larger cations, it is appropriate to compare them

Fig. 8 Atomic coordination of the M4 cation in grunerite **a** α-grunerite at ambient pressure **b** β-grunerite at 7.4(1) GPa **c** γ-grunerite at 22.8(4) GPa. Dashed lines indicate non-bonding and distances between atoms that are greater than 3 Å
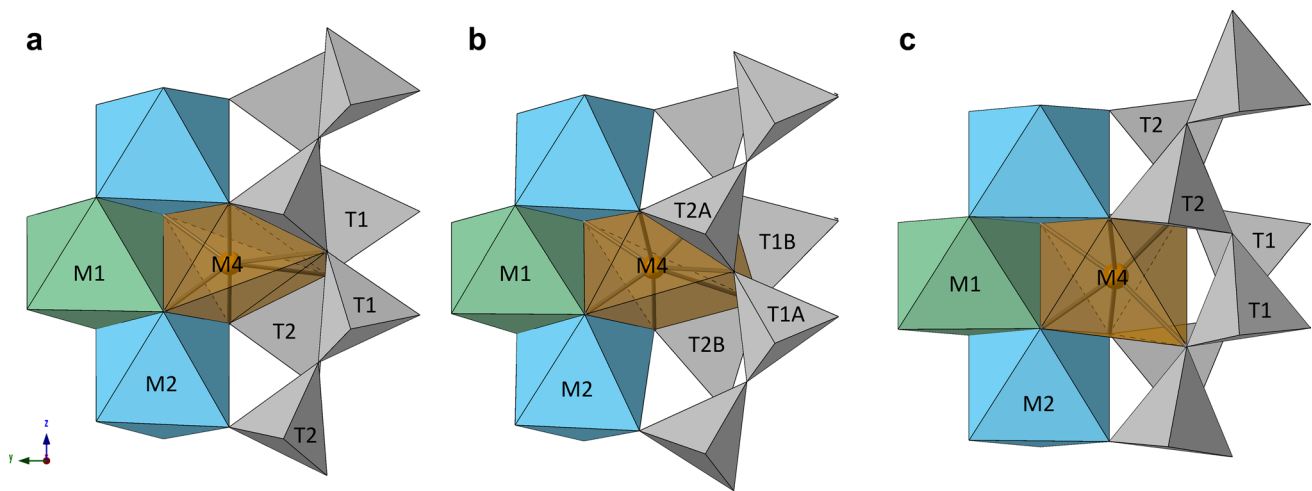
Fig. 9 M4 polyhedra configuration in grunerite. **a** α-grunerite at ambient pressure, M4 polyhedron sharing edges with M1, 2 × M2 and 2 × T2 polyhedra **b** β-grunerite at 7.4(1) GPa, M4 polyhedron sharing edges with M1, 2 × M2, T1B, T2A and T2B polyhedra **c** γ-grunerite at 22.8(4) GPa, M4 polyhedron sharing edges with M1 and 2 × M2 polyhedra

structural relations and demonstrates that the parallel phase transformation behavior is not only limited to temperature as proposed by Carpenter (1982), but also includes pressure. The high-temperature-$C2/c$ to $P2_1/c$ to high-pressure-$C2/c$ transformations in clinopyroxenes (Arlt et al. 2000; Nestola et al. 2008) is analogous to the α to β to γ-phase transition seen in this study. It is worth mentioning that in both clinopyroxenes and clinoamphiboles, high-pressure and high-temperature phase transitions have the same space group and both phases are isometric to each other (Tribaudino et al. 2001, 2003).

Equilibrium phase transformation sequences and chemical reactions experienced by the major rock forming minerals have been extensively studied and are well understood. Metastable transformations, however, are poorly constrained. Constraining the stability of these metastable phases is important, as they may have significant geophysical implications as suggested by Agrusta et al. (2014) and Tetzlaff and Schmeling (2000) for both olivine and pyroxene in subducting slabs. In the case of both these minerals, metastability promotes slab stagnation within the mantle transition zone due to the low-density metastable phases, which provide positive buoyancy effects (Agrusta et al. 2014). It is conceivable that this metastable phase of grunerite would exist in geologic environments such as the Tonga slab, where the thermal profile is lower than the mantle adiabat (Ganguly et al. 2009). It is estimated that the temperature of the Tonga slab within the mantle transition zone is less than 900 °C (Ganguly et al. 2009). The high-pressure and anomalously cold-temperature of this region may be a likely geologic environment where metastable amphiboles like γ-grunerite are preserved. The temperature in this region is near the upper limit of amphibole stability before dehydration occurs

(Wallace and Green 1991; Welch and Graham 1992; Konzett et al. 1997; Ernst and Liu 1998; Niida and Green 1999; Fumagalli and Poli 2005). The high-pressure, however, may have an effect of increasing the dehydration temperature. Constraining the stability of this metastable phase is important as it may have significant geophysical and petrological consequences, since amphiboles are commonly used as petrogenetic indicators and in geodynamic modelling. Phases similar to γ-grunerite may exist for other clino- and orthoamphiboles of different composition, therefore, further high-pressure investigations of these systems should be encouraged. In addition, simultaneous high-temperature and high-pressure studies on grunerite are needed to constrain the stability of γ-grunerite and to determine the dehydration temperature of this phase.

References

Agrusta R, Hunen J, Goes S (2014) The effect of metastable pyroxene on the slab dynamics. Geophys Res Lett 41:8800–8808

Alvaro M, Nestola F, Ballaran TB, Cámara F, Domeneghetti MC, Tazzoli V (2010) High-pressure phase transition of a natural pigeonite. Am Miner 95:300–311

Angel RJ (2000) High-pressure structural phase transitions. Rev Miner Geochem 39:85–104

Arlt T, Armbruster T (1997) The temperature-dependent $P2_1/c$-C2/c phase transition in the clinopyroxene kanoite $MnMg[Si_2O_6]$: a single-crystal X-ray and optical study. Eur J Miner 9:953–964

Arlt T, Angel RJ, Miletich R, Armbruster T, Peters T (1998) High-pressure $P2_1/c$–C2/c phase transitions in clinopyroxenes: influence of cation size and electronic structure. Am Miner 83:1176–1181

Arlt T, Kunz M, Stolz J, Armbruster T, Angel RJ (2000) P-T-X data on $P2_1/c$-clinopyroxenes and their displacive phase transitions. Contrib Miner Petrol 138:35–45

Boehler R, De Hantsetters K (2004) New anvil designs in diamond-cells. High Press Res 24:391–396

Boffa Ballaran T, Angel RJ, Carpenter MA (2000) High-pressure transformation behaviour of the cummingtonite-grunerite solid solution. Eur J Miner 12:1195–1213

Brown G, Prewitt C, Papike J, Sueno S (1972) A comparison of the structures of low and high pigeonite. J Geophys Res 77:5778–5789

Carpenter M (1982) Amphibole microstructures: some analogies with phase transformations in pyroxenes. Miner Mag 46:395–397

Comodi P, Mellini M, Ungaretti L, Zanazzi PF (1991) Compressibility and high pressure structure refinement of tremolite, pargasite and glaucophane. Eur J Miner 3:485–499

Comodi P, Ballaran TB, Zanazzi PF, Capalbo C, Zanetti A, Nazzareni S (2010) The effect of oxo-component on the high-pressure behavior of amphiboles. Am Miner 95:1042

Dera P (2007) GSE-ADA data analysis program for monochromatic single crystal diffraction with area detector. GeoSoilEnviroCARS, Argonne

Dera P, Zhuravlev K, Prakapenka V, Rivers ML, Finkelstein GJ, Grubor-Urosevic O, Tschauner O, Clark SM, Downs RT (2013) High pressure single-crystal micro X-ray diffraction analysis with GSE_ADA/RSV software. High Press Res 33:466–484

Dewaele A, Torrent M, Loubeyre P, Mezouar M (2008) Compression curves of transition metals in the Mbar range: experiments and projector augmented-wave calculations. Phys Rev B 78:104102

Downs RT (2003) Topology of the pyroxenes as a function of temperature, pressure, and composition as determined from the procrystal electron density. Am Miner 88:556–566

Ernst WG, Liu J (1998) Experimental phase-equilibrium study of Al- and Ti-contents of calcic amphibole in MORB; a semiquantitative thermobarometer. Am Miner 83:952–969

Finger LW (1969) The crystal structure and cation distribution of a grunerite. Miner Soc Am Spec Pap 2:95–100

Fumagalli P, Poli S (2005) Experimentally determined phase relations in hydrous peridotites to 6.5 GPa and their consequences on the dynamics of subduction zones. J Petrol 46:555–578

Ganguly J, Freed AM, Saxena SK (2009) Density profiles of oceanic slabs and surrounding mantle: integrated thermodynamic and thermal modeling, and implications for the fate of slabs at the 660 km discontinuity. Phys Earth Planet Inter 172:257–267

Gonzalez-Platas J, Alvaro M, Nestola F, Angel R (2016) EosFit7-GUI: a new graphical user interface for equation of state calculations, analyses and teaching. J Appl Crystallogr 49:1377–1382

Hawthorne FC, Oberti R (2007) Amphiboles: crystal chemistry. Rev Miner Geochem 67:1–54

Hirschmann M, Evans BW, Yang H (1994) Composition and temperature dependence of Fe–Mg ordering in cummingtonite-grunerite as determined by X-ray diffraction. Am Miner 79:862–877

Hugh-Jones D, Woodland A, Angel R (1994) The structure of high-pressure C2/c ferrosilite and crystal chemistry of high-pressure C2/c pyroxenes. Am Miner 79:1032–1041

Iezzi G, Liu Z, Della Ventura G (2006) Synchrotron infrared spectroscopy of synthetic $Na(NaMg)Mg_5Si_8O_{22}(OH)^2$ up to 30 GPa: Insight on a new high-pressure amphibole polymorph. Am Miner 91:479–482

Iezzi G, Liu Z, Della Ventura G (2009) Synthetic $^ANa^B(Na_xLi_{1-x}Mg_1)^CMg_5Si_8O_{22}(OH)_2$ (with x = 0.6, 0.2 and 0) $P2_1/m$ amphiboles at high pressure: a synchrotron infrared study. Phys Chem Miner 36:343–354

Iezzi G, Tribaudino M, Della Ventura G, Margiolaki I (2011) The high-temperature $P2_1/m \rightarrow C2/m$ phase transitions in synthetic amphiboles along the richterite–(^BMg)–richterite join. Am Miner 96:353

Konzett J, Sweeney RJ, Thompson AB, Ulmer P (1997) Potassium amphibole stability in the upper mantle: an experimental study in a peralkaline KNCMASH system to 8.5 GPa. J Petrol 38:537–568

Law AD, Whittaker EJW (1980) Rotated and extended model structures in amphiboles and pyroxenes. Miner Mag 43:565–574

Nestola F, Ballaran TB, Ohashi H (2008) The high-pressure C2/c–$P2_1/c$ phase transition along the $LiAlSi_2O_6$–$LiGaSi_2O_6$ solid solution. Phys Chem Miner 35:477–484

Nestola F, Pasqual F, Welch MD, Oberti R (2012) The effects of composition upon the high-pressure behaviour of amphiboles: compression of gedrite to 7 GPa and a comparison with anthophyllite and proto-amphibole. Miner Mag 76:987

Niida K, Green DH (1999) Stability and chemical composition of pargasitic amphibole in MORB pyrolite under upper mantle conditions. Contrib Miner Petrol 135:18–40

Papike JJ, Cameron M (1976) Crystal chemistry of silicate minerals of geophysical interest. Rev Geophys 14:37–80

Papike J, Ross M (1970) Gedrites-crystal structures and intracrystalline cation distributions. Am Miner 55:1945–1972

Prewitt CT, Downs RT (1998) High-pressure crystal chemistry. Rev Miner 37:283–318

Prewitt CT, Papike JJ, Ross M (1970) Cummingtonite: a reversible, nonquenchable transition from $P2_1/m$ to C2/m symmetry. Earth Planet Sci Lett 8:448–450

Rivers M, Prakapenka VB, Kubo A, Pullins C, Holl CM, Jacobsen SD (2008) The COMPRES/GSECARS gas-loading system for diamond anvil cells at the advanced photon source. High Press Res 28:273–292

Shannon R (1976) Revised effective ionic radii and systematic studies of interatomic distances in halides and chalcogenides. Acta Crystallogr Sect A 32:751–767

Sheldrick G (2008) A short history of SHELX. Acta Crystallogr Sect A 64:112–122

Smyth JR (1974) The high temperature crystal chemistry of clinohypersthene. Am Miner 59:1069–1082

Sueno S, Cameron M, Papike J, Prewitt C (1973) The high temperature crystal chemistry of tremolite. Am Miner 58:649–664

Tetzlaff M, Schmeling H (2000) The influence of olivine metastability on deep subduction of oceanic lithosphere. Phys Earth Planet Inter 120:29–38

Thompson EC, Campbell AJ, Liu Z (2016) In-situ infrared spectroscopic studies of hydroxyl in amphiboles at high pressure. Am Miner 101:706

Tribaudino M, Prencipe M, Nestola F, Hanfland M (2001) A $P2_1/c$–C2/c high-pressure phase transition in $Ca_{0.5}Mg_{1.5}Si_2O_6$ clinopyroxene. Am Miner 86:807–813

Tribaudino M, Nestola F, Meneghini C, Bromiley G (2003) The high-temperature $P2/c_1$–C2/c phase transition in Fe-free Ca-rich $P2_1/c$ clinopyroxenes. Phys Chem Miner 30:527–535

Wallace M, Green DH (1991) The effect of bulk rock composition on the stability of amphibole in the upper mantle: implications for solidus positions and mantle metasomatism. Miner Petrol 44:1–19

Warren B (1930) II. The structure of tremolite $H_2Ca_2Mg_5(SiO_3)_8$. Z Kristalogr Cryst Mater 72:42–57

Warren B, Modell D (1930) 11. The structure of anthophyllite $H_2Mg_7(SiO_3)_8$. Z Kristalogr Cryst Mater 75:161–178

Welch MD, Graham CM (1992) An experimental study of glaucophanic amphiboles in the system $Na_2O–MgO–Al_2O_3–SiO_2–SiF_4$ (NMASF): some implications for glaucophane stability in natural and synthetic systems at high temperatures and pressures. Contrib Miner Petrol 111:248–259

Welch MD, Cámara F, Ventura GD, Iezzi G (2007) Non-ambient in situ studies of amphiboles. Rev Miner Geochem 67:223–260

Welch MD, Gatta D, Rotiroti N (2011) The high-pressure behavior of orthorhombic amphiboles. Am Miner 96:623

Whittaker E (1960) The crystal chemistry of the amphiboles. Acta Crystallogr A 13:291–298

Yang H, Prewitt CT (2000) Chain and layer silicates at high temperatures and pressures. Rev Miner Geochem 41:211–255

Yang H, Hazen RM, Prewitt CT, Finger LW, Ren L, Hemley RJ (1998) High-pressure single-crystal X-ray diffraction and infrared spectroscopic studies of the $C2/m–P2_1/m$ phase transition in cummingtonite. Am Miner 83:288–299

Zanazzi PF, Nestola F, Pasqual D (2010) Compressibility of protoamphibole: a high-pressure single-crystal diffraction study of protomangano-ferro-anthophyllite. Am Miner 95:1758

Zhang L, Ahsbahs H, Kutoglu A, Hafner SS (1992) Compressibility of grunerite. Am Miner 77:480–483